Integrated approach to improve Road Infrastructure Resilience through complementary Non-Destructive Techniques

Alex Alonso-Díaz[1]; Mercedes Solla[1]; Juan Luis Rodríguez[1]; Ahmed Elseicy[1]

[1]CINTECX, GeoTECH Research Group. Universidade de Vigo - Alex.alonso@uvigo.es; merchisolla@uvigo.gal; jlsomoza@uvigo.gal; ahmedmossadibrahim.elseicy@uvigo.gal

Keywords: InSAR, GPR, GNSS, DEM, Pavement condition, digitalization.

Abstract

Transportation infrastructure serves as the backbone of societal functionality. As aging road networks present increasing challenges, effective monitoring and maintenance become imperative. In this context, this article explores the integration of non-destructive techniques for monitoring and assessing damaged road sections. The work emphasizes the importance of leveraging the complementarity between non-destructive techniques to gain a holistic understanding of damaged road sections' structural integrity. Through the combination of these techniques, structural issues and underlying causes can be identified, as well as to develop maintenance and rehabilitation strategies.
A case study of a critical section of the national road N-541 in Pontevedra, Spain, illustrates the application of this integration. First, Interferometry Synthetic Aperture Radar (InSAR) technology revealed points of interest. Four different cases, with two different methods: Scatterer Interferometry (PSI) and Quasi-PS (QPS) were used, to minimize uncertainty. Then, Global Positioning System (GPS) data, together with Laser Imaging Detection and Ranging (LiDAR), were used to create Digital Elevation Models (DEM). Finally, Ground Penetrating Radar (GPR) was useful to create a data cloud of possible subsurface damages. Machine learning technique (clustering) was applied to the GPR data to assist in defect depth analysis, further improving understanding and knowledge. The integration of complementary non-destructive methods offers a comprehensive framework for advancements in road infrastructure analysis and maintenance strategies, thus contributing to decision-makers to enhance transportation infrastructures' resilience and longevity.

1. Introduction

Transportation infrastructures, particularly roads, serve as the lifelines of modern societies, facilitating the movement of goods and people. The sustained functionality of these infrastructures is crucial for ensuring economic development, public safety, and overall societal well-being (Arbúes et al., 2015). As these road networks age, the need for effective monitoring and maintenance becomes increasingly paramount (Gagliardi et al., 2023). Timely and accurate assessment of the structural health of road sections is essential to prevent potential hazards, mitigate risks, and optimize resource allocation (D'Amico et al., 2020). This paper delves into the area of data integration and information fusion, focusing on the use of non-destructive techniques for monitoring and assessing damaged road sections.

Non-destructive techniques have emerged as invaluable tools in the realm of infrastructure monitoring, offering a non-intrusive means to evaluate the condition of pavements without causing further harm (Ip and Wang, 2011). Traditional assessment methods often require invasive procedures, leading to reliable results, but limited significance, disruptions in traffic flow, and increased costs and time (Gagliardi et al., 2023). Advances in non-destructive techniques, such as Interferometry Synthetic Aperture Radar (InSAR), Ground Penetrating Radar (GPR), LiDAR (Light Detection and Ranging), and infrared thermography provide detailed insights into the subsurface and surface conditions of road sections (Bianchini Ciampoli et al., 2020; Elseicy et al., 2022). However, these techniques are not yet considered as stand-alone analyses, and their complementarity enhances the comprehensiveness and accuracy of the collected data (D'Amico et al., 2020). This paper explores how the integration of diverse non-destructive methods can offer a holistic understanding of the structural integrity of damaged road sections, supporting effective decision-making in maintenance and rehabilitation strategies.

The synergy between non-destructive techniques in pavement monitoring not only aids in identifying structural issues but also enables a comprehensive analysis of the underlying causes (Alonso-Díaz et al., 2023a). Different techniques excel in capturing specific aspects of pavement conditions, such as the detection of voids, moisture content, subsidence patterns, bearing capacity, or layer thickness (Elseicy et al., 2022). By combining these techniques, practitioners gain a better understanding of the multifaceted challenges faced by damaged road sections. This paper highlights the importance of leveraging the complementarity between non-destructive techniques to harness a wealth of information, fostering a more informed and efficient approach to the analysis of road infrastructure. The goal is to provide a comprehensive framework for decision-makers to enhance the resilience and longevity of transportation infrastructures.

The article is organized as follows: Section 2 presents the previous works, the study area, as well as the methodology of each of the techniques used. The results obtained with 2D and 3D viewing, as well as their discussion, are presented in Section 3. Finally, conclusions and future perspectives are included in Section 4.

2. Materials and Methodologies

2.1 Previous work

The non-destructive techniques can only provide partial analysis due to their limitations. The data fusion of multi-scale information that works at different levels is a practical methodology that can overcome these limitations. There are no works combining all these techniques over the same area, but some investigations have studied the pavement condition with some of them: i) GPR and InSAR (Alonso-Díaz et al., 2023a), (Alonso-Díaz et al., 2023b) and (Bianchini Ciampoli et al., 2020); ii) GPR and LiDAR (Saarenketo et al., 2019); iii) InSAR and LiDAR (D'Aranno et al., 2019).

This contribution has been peer-reviewed. The double-blind peer-review was conducted on the basis of the full paper.
https://doi.org/10.5194/isprs-annals-X-4-W5-2024-9-2024 | © Author(s) 2024. CC BY 4.0 License.

2.2 Case study

This case study focuses on a critical section of the national road N-541, situated in the city of Pontevedra (Galicia, Spain), close to the Lerez River (Figure 1). Specifically, this section serves as access to the Bridge "Os Tirantes".

The area is under river flooding risk with a period of flood occurrence of 10 years, with water depth associated with each point in our case study not exceeding 0.1 meters (SNCZI-IPE, 2024). The significance of this section lies in its heavy use by both pedestrians and vehicles, putting a population at risk within the flood zone estimated between 1 and 100 inhabitants (SNCZI-IPE, 2024), derived from the *Sistema Nacional de Cartografía de Zonas Inundables* (SNCZI) in collaboration with the *Instituto de Productos y Servicios* (IPE).

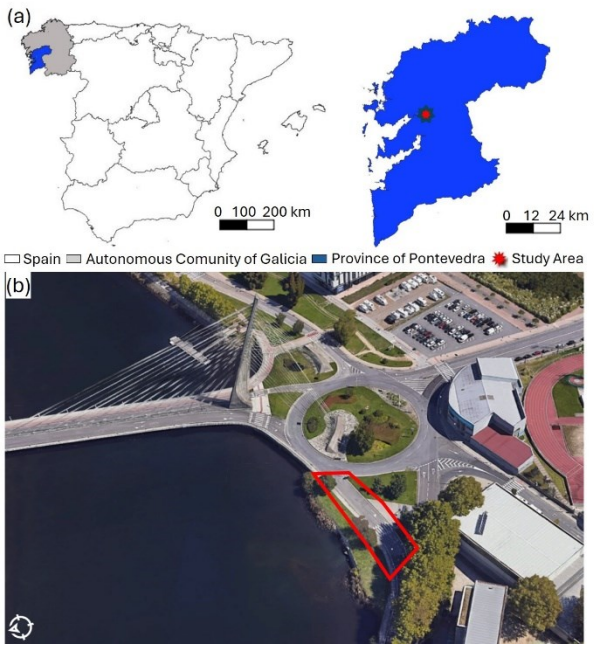

Figure 1. a) Study area map location, b) 3D view of the area marking the studied road section (highlighted into a red box).

The studied section of the road underwent visual monitoring to assess its condition and evolution (Figure 2). A noticeable increase in wear and tear was observed, leading to the decision to repave the road after this on-site data collection (Faro de Vigo newspaper, 2020). To improve the analysis, additionally information was compiled, documenting the damages and elements present on the road, including alligator cracking, longitudinal and transversal cracks, patching, speed bumps, storm drains, catch basins, and a water treatment plant.

Figure 2. Visual images overtime on the road section.

2.3 InSAR

InSAR technology achieves, in specific cases, sub-millimeter precision of surface deformation (Bianchini Ciampoli et al., 2020). This technique is applied to the study area to monitor, through temporal series of highly coherent scatters, how it has behaved over time. Initially, the results of the vertical component of the ortho product from the European Ground Motion Service (EGMS) grid (Copernicus, 2021a) encompassing our study area are visualized. As a result, the area shows a pronounced trend of subsidence (-1,4 mm/year mean velocity) in the vertical component (Figure 3).

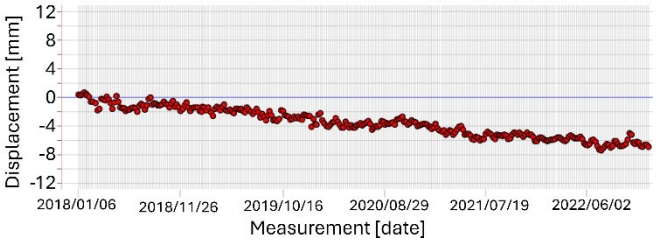

Figure 3. Time-series of the vertical component of ortho product for the grid over the area of study.

Four cases of InSAR technology have been conducted in two temporal lines over the study area. The images used were from Sentinel-1 constellation A/B, C-band and polarization VV+VH. These images were selected because this sensor is open source and presents the correct balance between decorrelation and resolution in a mixed environment like this one (urban area with vegetation).

Timeline	12/03/2021-07/03/2022		04/01/2020-30/03/2022	
Number of Interferograms	48	250	120	405
Orbit	Ascending		Descending	
Master image	08/10/2021	-	10/01/2021	-
Software	SARPROZ			
Method	PSI	QPS	PSI	QPS
Swath	2			
Incidence angle	37,0-37,5º			
Scatters in road section	3		2	

Table 1. Information about the different InSAR cases.

The reason for conducting these four cases is to reduce the uncertainty associated with this technology. By examining cases with different temporalities, the impact of coherence loss is minimized. Obtaining results for both orbits helps mitigate the effects of shadowing and foreshortening (Figure 4a). Ultimately, employing different methods contributes to error reduction, helps to evaluate seasonal effects and reduces the importance of the master image (Figure 4).

Figure 4 represents the study conducted to assess the spatial correction of InSAR results and ensure proper referencing. Temporal series of consistent scatters were graphed based on the employed methods (Figure4b,c) to evaluate the spatial correctness and appropriateness of referencing. After checking the accumulated difference between time series configurations, for the descending orbit, it averages a difference of 5 mm between the PSI and SqueeSAR methods, while between QPS and PSI the difference is around 8 mm, along the Line-of-Sight (LOS). Within this value, all possible differences (processing, algorithms, and referencing) are included. It can be inferred that QPS does not include a seasonal component as it lacks seasonal trends. For the ascending orbit, with fewer data points (48

This contribution has been peer-reviewed. The double-blind peer-review was conducted on the basis of the full paper.
https://doi.org/10.5194/isprs-annals-X-4-W5-2024-9-2024 | © Author(s) 2024. CC BY 4.0 License.

interferograms), the accumulated difference is around 2 mm between QPS and SqueeSAR and close to 3 between PSI and SqueeSAR showing the dual behavior of the SqueeSAR algorithm (Distributed target-Point like scatterer) (Copernicus, 2021b).

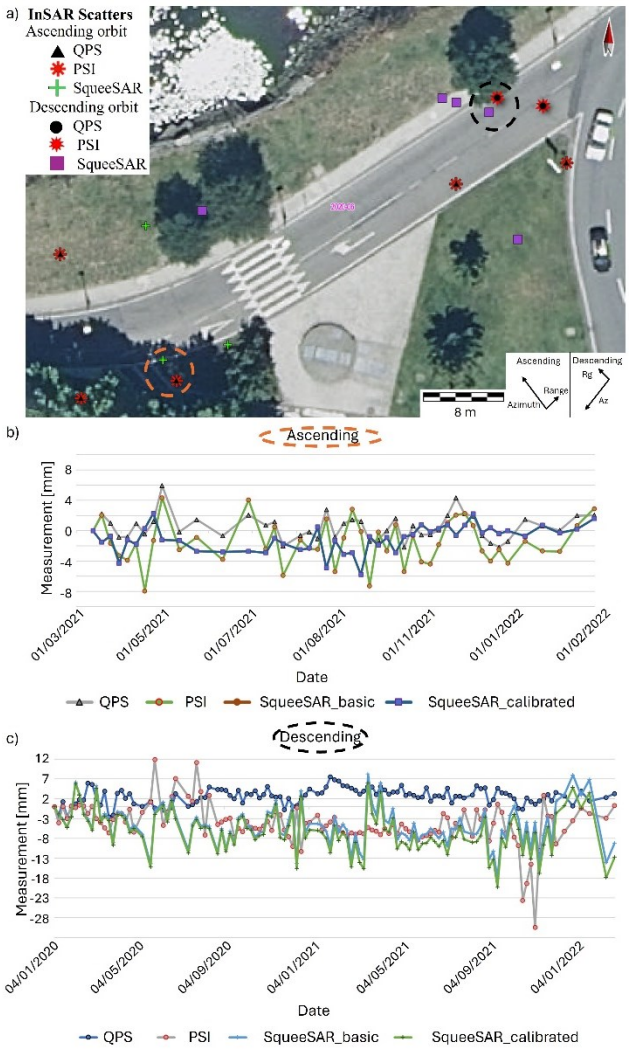

Figure 4. a) InSAR scatters obtained for each configuration, b) Scatter time-series of each method for ascending orbit (into dashed green circle), c) Scatter time-series of each method for descending orbit (scatters into black dashed circle).

2.4 Digital elevation model (DEM)

The GNSS receiver used was a Trimble R8 Model that receives GNSS data from the NAVSTAR and GLONASS constellations, and with precision in differential code positioning of 0.25 meters horizontally and 0.5 meters vertically, and in RTK (Real Time Kinematic) positioning of 10 millimeters horizontally and 20 millimeters vertically.

Two digital elevation models were created: i) based on GPS data obtained during the test (June 2022) with a total of 583 points; and ii) based on LiDAR data obtained in the second coverage by IGN [12] (2015) with a total of 640 points. As shown in Figure 5, after processing (cutting, rectifying and filtering) the primary data, comparable results were obtained.

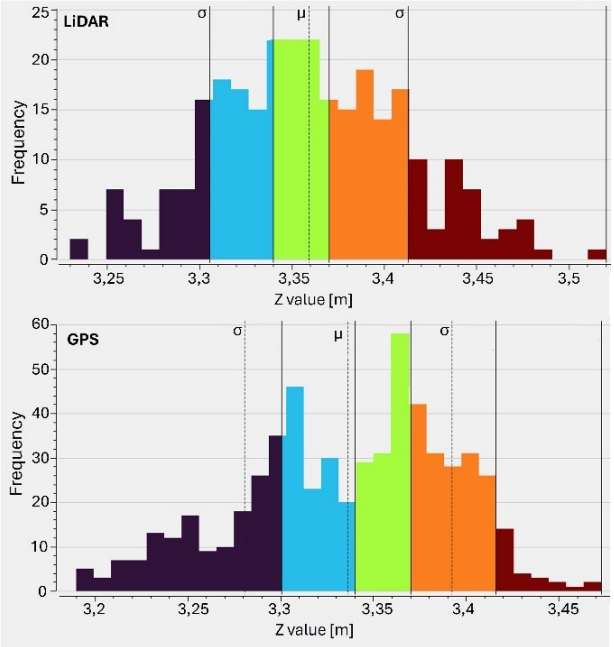

Figure 5. Histogram of the Z values for LiDAR data (up) and GPS measurements (down).

To create the DEMs it was necessary to do triangulation between points and interpolation between the triangulated measurements to obtain the rasters (Figure 6).

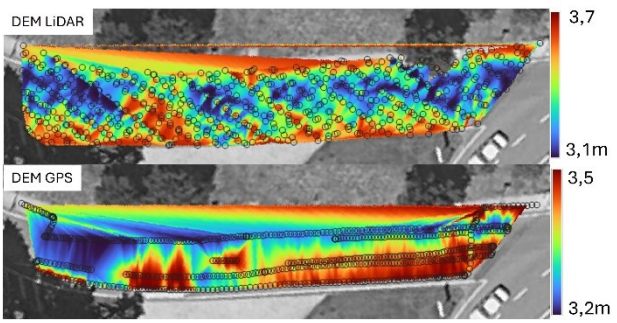

Figure 6. DEM created from LiDAR data (up) and GPS measurements (down) showing the points with Z information.

To assess the significance of information collected at different times, new rasters were generated using a common base, which is the 2010 first coverage LiDAR data from IGN (Figure 7).

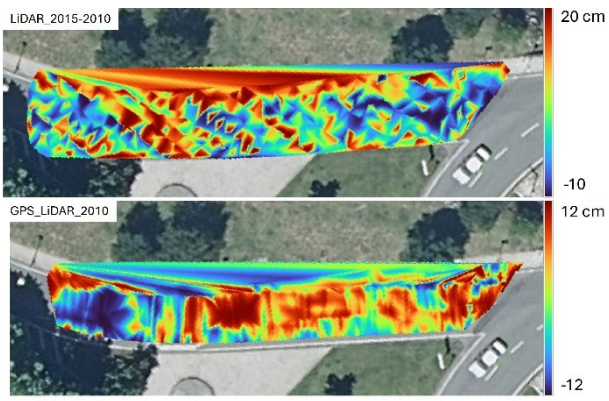

Figure 7. Difference between LiDAR 2015 and 2010 (up) and difference raster between GPS and LiDAR 2010 (down).

Finally, to visualize the similarities and differences between both DEMs, Figure 8 illustrates the 3D representations.

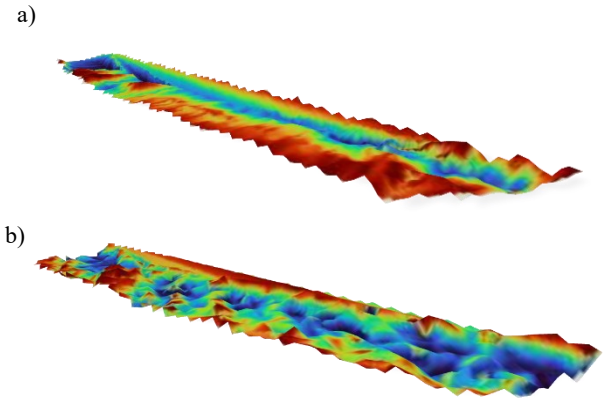

Figure 8. 3D model of the DEM, a) based on GPS and b) based on LiDAR data.

2.5 Ground Penetrating Radar

Seven GPR profile lines were gathered along the test site (Figure 9) using a ProEx system from Malå Geoscience, with a 500 MHz center frequency antenna. Table 2 shows the setting parameters used for data acquisition. Additionally, the external Trimble R8 GPS was connected to the GPR for trace tagging, so the GPR traces were recorded with RTK corrected coordinates. The GPR system was installed on a survey cart that incorporated an odometer wheel for measuring profile lengths and maintaining trace distance control (Figure 10). The protocol NMEA (GGA sentence) was used for GPR-GPS synchronization to provide 3D coordinates and accuracy data.

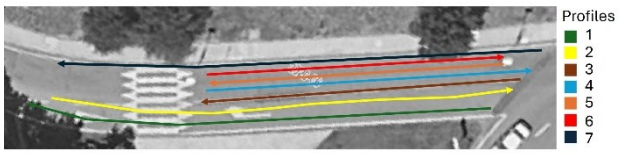

Figure 9. Layout of the 7 profiles captured.

Acquisition date	30/06/2022
Frequency antenna	500 MHz
Distance interval	0,02 m
Total time window	80 ns

Table 2. Information of the GPR test configuration.

Figure 10. Data collection and GPR-GPS system setup.

The B-scans (or radargrams) generated were processed using the ReflexW software, by applying the following processing sequence: time-zero correction, subtract-mean (dewow), linear and exponential gain function, background removal, and bandpass filtering (butterworth).

Then, Figure 11 shows the GPR data digitization methodology assumed to extract the elements of interest (Figure 11): First, the reflections of interest (pipes, damages and pavement changes) were drawn on the B-scans (green lines). For each reflection, we extracted the corresponding traces (horizontal positioning) and their respective depths (vertical positioning), which were computed using a standard signal velocity of propagation of 10 cm/ns. Then, all the data was extracted as an ASCII file (one file for each profile line), providing information about the extent and depth of the potential targets. Finally, the exported traces were associated with their GPS coordinates, creating a CSV file to be later imported into a GIS environment.

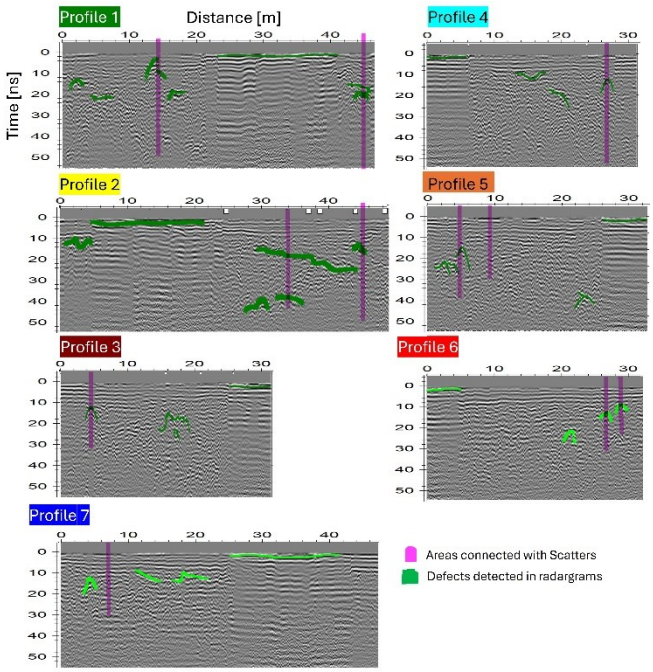

Figure 11. Radargrams of the different profiles interpreted and scatter locations from the InSAR study.

3. Results and discussion

The results are presented in two different ways: i) a 2D representation, in which the different layers of information are gradually displayed (Figure 12), and ii) a 3D representation, which is more visual and allows to connect the different layers of information.

3.1 2D representation

Figure 12 presents the results in a 2D form. Figure 12a illustrates a total of 6 surface distresses identified during visual inspection (one longitudinal and three transversal cracks, one alligator cracking and patching). The presence of utilities (catch basins and storm drains) is also included in this layer. Additionally, the InSAR scatters, obtained from the different configurations tested, are displayed on the same plane.

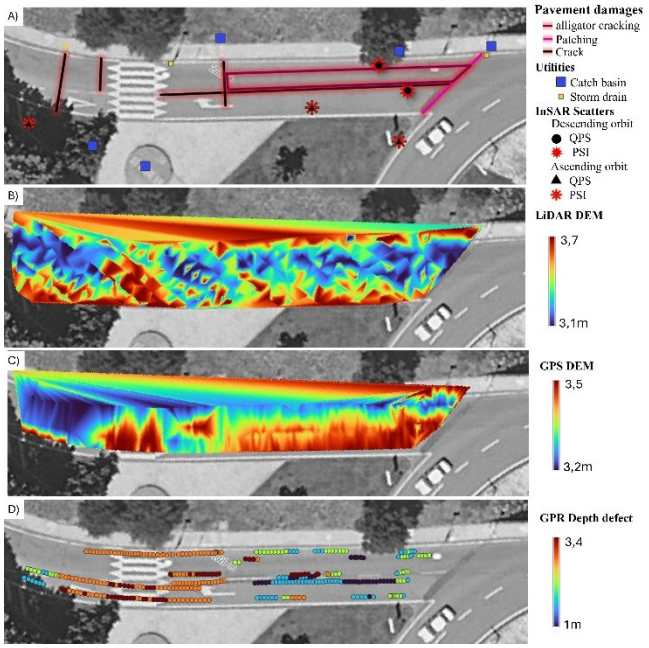

Figure 12. Layers of information: a) visual inspection (surface elements of interest), and InSAR results; b) LiDAR DEM; c) GPS DEM; and d) GPR layer with objects locations and depths.

Figure 12b shows the DEM obtained from LiDAR data according to height information (to use the same reference system), while Figure 12c presents the DEM obtained from GPS data. Both models have similar results: i) present comparable value scale, ii) detect road grade, iii) find a rumble strip, iv) general pattern, v) have a greater drop angle towards the storm drains, and vi) the minimum values are found after the speed bump, although they were obtained at different times and the density and allocation of points are different.

Figure 12d presents the subsurface defects detected with the GPR technique, using a depth scale (colormap code in reference to global height information), where red colours inform about superficial defects and blue colours report deeper defects. This map, together with the radargrams, provides information about the subsurface condition, highlighting: i) the probable presence of a pipeline that crosses the street close to the roundabout (green points), ii) the connection between surface cracks with deep defects (subgrade soil problem or internal damage), iii) the relationship between GPS DEM (the isolated high elevation value before the speed bump) and surface failure, iv) the agreement between DEM limit change and deep failures, v) the possible relation between longitudinal crack with surface failures and transversal cracks with deep ones (purple and blue points in the GPR layer), and vi) the relation between descending orbit InSAR scatters with evident damages and contrasted with GPR analysis (deep failures). However, the scatters obtained from ascending orbit are also associated with GPR proved defects, but not with visual failures.

3.2 3D representation

Figure 13 presents all the information layers into a 3D view for better visualization and understanding.

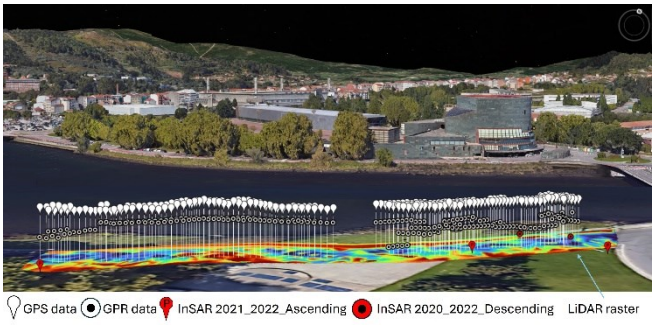

Figure 13. 3D representation of the different information layers.

Finally, the results are represented using Python, and machine learning techniques were applied to derive new insights. Aiming to group the GPR points, the clustering method using the K-Means class from the Scikit-learn library was applied. After applying the elbow method (a graph that presents the inertia for each possible number of clusters, Figure 14). The inertia is the distance root mean square of each instance to its nearest centroid, the inflection point is around 2 or 3 clusters. Considering domain knowledge, it was decided to use 3 clusters, related to the depth of the defects. Figure 15 shows the representation of the three techniques from different orientations to enhance the understanding of the analysis. The connection between the InSAR scatters and the clusters of GPR faults is evident, except for the shallower faults associated with the speed bump.

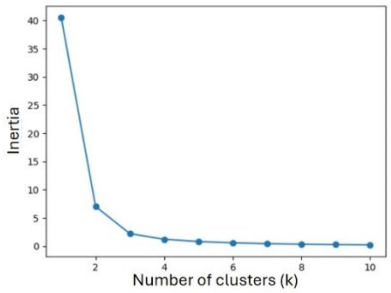

Figure 14. Elbow method results to determine number of clusters.

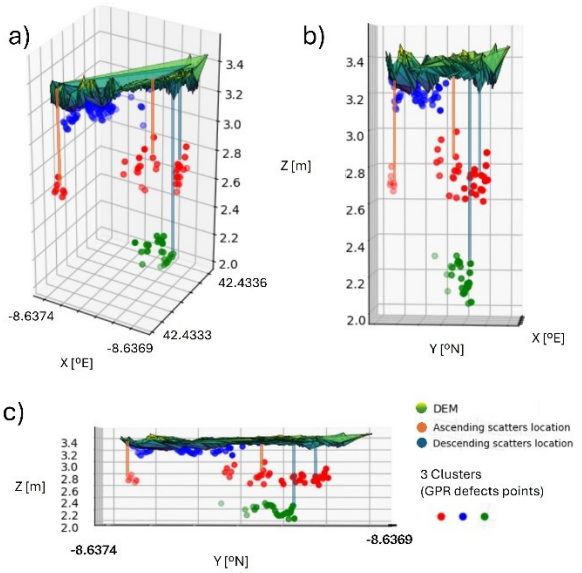

Figure 15. Joint representation of the results including the clusters related to the GPR point cloud: a) military, b) predominantly slanted knight's and c) frontal perspectives.

4. Conclusions and future perspectives

A section of road with a high risk of flooding and heavy pedestrian and vehicular traffic has been studied. Visible faults in the section have worsened over time, leading to repaving after data collection. Layers of information about the study area were stacked, including lists of visible faults and elements, digital elevation models, points of interest from InSAR technology, and georeferenced GPR point clouds associated with possible subsurface failures.

Four MT-InSAR cases with different configurations were conducted, demonstrating their complementarity. Two digital elevation models based on LiDAR and GPS data from different dates were created and their results were compared, highlighting their similarities when referenced to baseline data. GPR profiles were conducted, processed, interpreted, and georeferenced, resulting in a point cloud of possible subsurface faults.

The different layers were visualized in both 2D and 3D formats for a better understanding and analysis. From the 2D analysis, the following insights were extracted: i) spatial connection between descending orbit scatters and visible faults, ii) detection of road gradients and speed bumps based on digital elevation models, iii) connection between longitudinal cracks and surface GPR defects, and transverse cracks with deeper faults, and iv) relationship between deep GPR faults and InSAR scatters.

Finally, the 3D representation provided more insights to the relationship between the InSAR scatters detected and the deep GPR faults interpreted. It was possible by applying cluster analysis to the GPR point cloud, grouping them into three blocks and differentiating GPR faults into three height levels. Future works would require the automation of GPR data georeferencing and target detection.

About the different technologies, all of them provide extra layers of information: i) InSAR informs, from a space-level perspective, about points of interest (subsidence, bumping, seasonality, time-series evolution and coherence); ii) GNSS provides georeferentiation for the other techniques, and together with LiDAR obtains DEMs (3D models) from a sky-level perspective; and iii) GPR informs, from a ground-level perspective about the subsurface.

Another advantage of this methodology is the economic point of view. InSAR and LiDAR data come from open sources (exists also costly options to improve their performance). The drawbacks are the experience necessary to acquire the results, the on-situ tests and the GPR-GNSS equipment acquisition.

To sum up, in this case, the combination of InSAR-GNSS-GPR provides multiscale complementary information and LiDAR data obtained similar results to GNSS corroborating the other techniques' results.

Acknowledgements

This work has received financial support from the STRADAR project (TED2021-130183B-I00) funded by MCIN/AEI/10.13039/501100011033 and by the “European Union NextGenerationEU/PRTR”. A. Alonso-Díaz acknowledges the funding received from the Xunta de Galicia through the ENDITí project (ED431F 2021/08). M. Solla acknowledges the Grant RYC2019–026604–I funded by MCIN/AEI/10.13039/501100011033 and by “ESF Investing in your future”. A. Elseicy acknowledges the Grant PREP2022-000030 for the training of predoctoral researchers funded by MCIN/AEI /10.13039/501100011033 and by FSE+.

References

Algorithm Theoretical Basis Document, 2021, End-to-end implementation and operation of the European Ground Motion Service (EGMS). https://land.copernicus.eu/en/technical-library/egms-algorithm-theoretical-basis-document

Alonso-Díaz, A., Solla, M., Fontul, S., Marecos, V., de Lurdes Antunes, M., & Pais, J. C. (2023a, July). A Non-Invasive and Multi-Scale Approach to Detect Subsidence in Pavements: InSAR, FWD and GPR. In 2023 12th International Workshop on Advanced Ground Penetrating Radar (IWAGPR) (pp. 1-4). IEEE.

Alonso-Díaz, A., Solla, M., Elseicy, A., & Rodríguez, J. L. (2023b, July). The Complementarity of GPR and MT-InSAR for Pavement Damage Monitoring: Preliminary Results. In 2023 12th International Workshop on Advanced Ground Penetrating Radar (IWAGPR) (pp. 1-4). IEEE.

Arbués, P., Baños, J. F., & Mayor, M. (2015). The spatial productivity of transportation infrastructure. *Transportation Research Part A: Policy and Practice*, 75, 166-177.

Bianchini Ciampoli, L., Gagliardi, V., Clementini, C., Latini, D., Del Frate, F., & Benedetto, A. (2020). Transport infrastructure monitoring by InSAR and GPR data fusion. *Surveys in Geophysics*, 41, 371-394.

Copernicus, European Ground Motion Service, Accessed on: January 2024. https://egms.land.copernicus.eu/

D'Amico, F., Gagliardi, V., Ciampoli, L. B., & Tosti, F. (2020). Integration of InSAR and GPR techniques for monitoring transition areas in railway bridges. *NDT & E International*, 115, 102291.

D’Aranno, P., Di Benedetto, A., Fiani, M., & Marsella, M. (2019). Remote sensing technologies for linear infrastructure monitoring. *International Archives of the Photogrammetry, Remote Sensing and Spatial Information Sciences*, 42, 461-468.

Elseicy, A., Alonso-Díaz, A., Solla, M., Rasol, M., & Santos-Assunçao, S. (2022). Combined use of GPR and other NDTs for road pavement assessment: An overview. *Remote Sensing*, 14(17), 4336.

Gagliardi, V., Tosti, F., Bianchini Ciampoli, L., Battagliere, M. L., D’Amato, L., Alani, A. M., & Benedetto, A. (2023). Satellite remote sensing and non-destructive testing methods for transport infrastructure monitoring: Advances, challenges and perspectives. *Remote Sensing*, 15(2), 418.

Ip, W. H., & Wang, D. (2011). Resilience and friability of transportation networks: evaluation, analysis and optimization. *IEEE Systems Journal*, 5(2), 189-198.

La empresa inicia los trabajos de reposición del firme en la avenida de Buenos Aires, Faro de Vigo newspaper, November 2020. Accessed on: January 2024. https://www.farodevigo.es/pontevedra/2020/10/08/empresa-inicia-trabajos-reposicion-firme-20188066.html

Saarenketo, T., & Silvast, M. (2019). Using laser scanner and GPR data in geotechnical diagnostics of roads and railways. 17th European Conference on Soil Mechanics and Geotechnical Engineering, ECSMGE 2019.

Sistema Nacional de Cartografía de Zonas Inundables Inventario de Presas y embalses (SNCZI-IPE map). Accessed on: January 2024. https://sig.mapama.gob.es/snczi/